Examination of three-dimensional effects using a propagation model with azimuth-coupling capability (FOR3D)

Ding Lee and George Botseas
Naval Underwater Systems Center, New London, Connecticut 06320

William L. Siegmann
Rensselaer Polytechnic Institute, Troy, New York 12180

(Received 8 May 1989; revised 1 January 1992; accepted 17 February 1992)

A three-dimensional wave propagation model of parabolic approximation type (FOR3D) is used to examine 3-D ocean environmental variations. The background theory and characteristics of the model are reviewed briefly. Propagation situations that are classified as 3-D, $N \times 2$-D, and 2-D are described in connection with FOR3D and are interpreted in several ways. An analytic exact solution is used to demonstrate the model's accuracy and its capability for treating fully 3-D propagation, when coupling exists between solutions in adjacent vertical planes of constant azimuth. It is also employed to illustrate a procedure for using approximate conditions at vertical side boundaries in a 3-D calculation. An application is made to an Atlantic Ocean shelf-slope environment with realistic bottom topographic variations and sound-speed profiles. The occurrence of significant azimuthal coupling is demonstrated in propagation loss versus range curves. It follows that, while the $N \times 2$-D approximation of no azimuthal coupling is useful in many situations, not all 3-D ocean acoustics problems can be adequately solved without a fully 3-D propagation model.

PACS numbers: 43.30.Bp

INTRODUCTION

One basic issue in the investigation of oceanic sound propagation is to what extent the propagation under given conditions is three dimensional (3-D). With a cylindrical coordinate representation, having z as depth and the source on the line $r = 0$, fully 3-D propagation refers to that involving azimuthal or θ coupling. That is, the propagation in at least one vertical plane of constant azimuth is coupled to that in another such plane. It is clear that when θ coupling is negligible or absent, there is no need to use a propagation model with full 3-D capability, and a two-dimensional (2-D) model is sufficient. It is also obvious that when θ coupling is non-negligible, models without 3-D capability will not produce correct results.

Most ocean acoustic wave propagation problems have been solved to date by 2-D models. However, this should not be taken to imply that all problems can be solved by 2-D models, or that an accurate 3-D model is not necessary. Perhaps the first serious examinations of the 3-D influences of ocean volume effects, i.e., sound-speed variations, on lower-frequency propagation reported only relatively small influences.[1,2] Other work, for example Ref. 3, suggests the importance of bottom topographic variations on 3-D propagation. The significance of the mechanism has been confirmed by 3-D computations in shallow-water environments.[4,5] These simulations, obtained by a different parabolic approximation from that in Refs. 1 and 2, demonstrate the usefulness of one-way methods for analysis of 3-D propagation.

Progress has been made on development of an accurate and fully capable 3-D model for one-way, low-frequency propagation. A new 3-D wide-angle wave equation was described in Ref. 6, along with an efficient numerical scheme as a marching method with unconditional stability. The efficiency of the method is due to the fact that marching from one range to the next requires solution of only two tridiagonal systems of equations via recursive formulas. In the event that θ coupling is absent, only one tridiagonal system needs solution. The method has been implemented[7] into a research code with the acronym FOR3D, and some initial testing has been reported.[8] Examinations of fully 3-D acoustic propagation can be performed, whenever adequate environmental information and data is at hand. An upgrade has been made in the original FOR3D implementation in order to include density changes in the sediment layers.[9] We illustrate in this paper the influence of sediment density in a situation where θ coupling is present. Comprehensive investigations of situations with both 3-D volume and 3-D boundary variations have only recently been initiated, partly due to the lack of accurate and capable 3-D propagation models. Models which address various aspects of 3-D ocean sound propagation include a ray-based development,[10] mode-based procedures[11,12] along with special solutions,[13] other parabolic approximation methods,[4,5,11] a finite-element algorithm,[14] and a boundary integral method.[15]

In Sec. I, we give a brief outline of the mathematical development behind FOR3D, its numerical marching scheme, and its computer implementation. Then, in Sec. II, a discussion of θ coupling and θ dependence is given for 3-D, $N \times 2$-D, and 2-D versions of FOR3D. Interpretations are presented from mathematical, computational, and physical

 0001-4966/92/063192-11$00.80

points of view. In Sec. III, two computational examples are discussed, both based on a closed form exact solution. The first is used to test accuracy of FOR3D and to show its capability for handling θ coupling. The second is useful to validate a procedure for applying approximate conditions at vertical side boundaries in a 3-D calculation. In Sec. IV, we use realistic sound-speed profiles and bottom topography from the Harvard Oceanography group to show the occurrence of significant θ coupling in a representation of an actual ocean environment. Methods for assuring numerical convergence of 3-D solutions are discussed and illustrated. Section V is a brief summary.

I. THREE-DIMENSIONAL WIDE-ANGLE MODEL FOR3D

A mathematical model of outgoing acoustic propagation, developed in Ref. 6, is a high-order partial differential equation incorporating variations in three spatial dimensions. The model accounts for wide-angle coupling in the vertical (z) direction and narrow-angle coupling in the azimuthal (θ) direction, with propagation in the radial (r) direction. The solution of this mathematical model is by means of an efficient numerical method through a marching procedure, described in Ref. 7. The research computer code incorporates useful capabilities and offers a number of options. A brief description of the model is provided in this section, with full details available in the aforementioned references. The discussion here provides essential background for the interpretations in Sec. I and the applications to 3-D problems in Secs. III and IV.

We start from the standard 3-D Helmholtz equation for acoustic pressure, neglecting density variations. As in Refs. 6 and 7, we define the operators

$$X = \frac{1}{k_0^2}\frac{\partial^2}{\partial z^2} + n^2(r,\theta,z) - 1 \tag{1}$$

and

$$Y = \frac{1}{k_0^2 r^2}\frac{\partial^2}{\partial \theta^2}, \tag{2}$$

where as usual k_0 is the reference wave number and $n(r,\theta,z)$ is the index of refraction. After the far-field approximation, standard procedures lead to the following equation for the pressure envelope function $u(r,\theta,z)$:

$$u_{rr} + 2ik_0 u_r + k_0^2(X+Y)u = 0. \tag{3}$$

Equation (3) is factored, assuming weak variations to allow operator commutativity, and only the factor accounting for outgoing propagation is retained. With a particular definition of the resulting square root, the following high-order wave equation is obtained:

$$u_r = ik_0\left[-1 + (1 + \tfrac{1}{2}X - \tfrac{1}{8}X^2 + \tfrac{1}{2}Y)\right]u. \tag{4}$$

Equation (4) can be referred to as the Lee–Saad–Schultz (LSS) outgoing wave equation. We note that the LSS equation may also be derived by a multiscale asymptotic formalism.[8,16] This method of derivation shows that Eq. (4) is a consistent approximation for wide-angle propagation in the vertical direction and narrow-angle propagation in azimuth. Moreover, the portion $1 + X/2 - X^2/8$ corresponds exactly to the wide-angle capability described in Ref. 17 for the 2-D case.

An ordinary differential equation method is applied to solve Eq. (4), so that the solution can be expressed explicitly:

$$u(r+\Delta r,\theta,z) = e^{-\delta}\exp\left[\delta(1 + \tfrac{1}{2}X - \tfrac{1}{8}X^2 + \tfrac{1}{2}Y)\right]u(r,\theta,z), \tag{5}$$

where $\delta = ik_0\,\Delta r$. Exploiting again the slow variation of the index of refraction, the operators X and Y are nearly commutative, so that Eq. (5) becomes

$$u(r+\Delta r,\theta,z) = e^{-\delta}\exp\left[\delta(1 + \tfrac{1}{2}X - \tfrac{1}{8}X^2)\right]e^{(\delta/2)Y}u(r,\theta,z). \tag{6}$$

The requirement of near commutativity is achieved computationally by using sufficiently small increments.

The key to obtaining an efficient computation scheme for Eq. (6) is the use of rational function approximations to both exponentials:

$$\exp\left[\delta\left(1 + \frac{1}{2}X - \frac{1}{8}X^2\right)\right] = e^{\delta}\left(\frac{1 + (\frac{1}{4} + \delta/4)X}{1 + (\frac{1}{4} - \delta/4)X}\right) \tag{7}$$

and

$$e^{(\delta/2)Y} = \frac{1 + (\delta/4)Y}{1 - (\delta/4)Y}. \tag{8}$$

Since δ is purely imaginary and X and Y are self-adjoint operators, the denominators in Eqs. (7) and (8) are nonsingular. From these two equations, a marching procedure can be developed that has the formula

$$\left[1 + \left(\frac{1}{4} - \frac{\delta}{4}\right)X\right]\left(1 - \frac{\delta}{4}Y\right)u^{j+1} = \left[1 + \left(\frac{1}{4} + \frac{\delta}{4}\right)X\right]\left(1 + \frac{\delta}{4}Y\right)u^{j}, \tag{9}$$

where superscript j denotes the index of the range increment (later in this section, subscripts m and l will indicate depth and azimuthal increments, respectively). Equation (9) may be used as the basis for a marching method which is unconditionally stable.[6]

The use of Eq. (9) to solve the LSS equation requires a finite difference scheme. This was developed by decomposing Eq. (9) into two steps, namely,

$$\text{Step 1:}\quad \left[1 + \left(\frac{1}{4} - \frac{\delta}{4}\right)X\right]w^{j+1} = \left[1 + \left(\frac{1}{4} + \frac{\delta}{4}\right)X\right]\left(1 + \frac{\delta}{4}Y\right)u^{j}, \tag{10}$$

$$\text{Step 2:}\quad \left(1 - \frac{\delta}{4}Y\right)u^{j+1} = w^{j+1}. \tag{11}$$

With a three-point differencing of the operators X and Y, it follows that Eqs. (10) and (11) lead to two tridiagonal linear systems at each range step. This is a principal advantage of our FOR3D implementation, since numerical solution of tridiagonal systems can be performed very efficiently.

Azimuthal coupling is treated by FOR3D via the approximation of the operator Y in Eqs. (10) and (11). We observe that if θ coupling is absent or negligible, Eq. (11)

reduces to $u^{j+1} = w^{j+1}$. In this case, only a single tridiagonal system, Eq. (10), needs to be solved. This observation is connected to a categorization of propagation cases, to be discussed in the next section.

II. 3-D, $N\times$2-D, 2-D PROPAGATION

We describe a classification of problems based on the influence of azimuthal variations. The FOR3D implementation deals with the solution of Eq. (4), or equivalently of the equation

$$\text{3-D:}\quad u_r = (ik_0/2)(X - \tfrac{1}{4}X^2 + Y)u. \tag{12}$$

This is the appropriate equation to be used in the fully 3-D problem, when *θ coupling is present*. In contrast, when *θ coupling is negligible but θ dependence is present*, the appropriate equation is

$$N\times\text{2-D:}\quad u_r = (ik_0/2)(X - \tfrac{1}{4}X^2)u. \tag{13}$$

Note that θ dependence appears only in the index of refraction in the operator X [see Eq. (1)]. The $N\times$2-D terminology was introduced in Ref. 2 to denote the solution of (uncoupled) 2-D propagation problems in N vertical planes. Finally, if *both θ coupling and θ dependence are negligible*, the problem is strictly 2-D. The appropriate equation is

$$\text{2-D:}\quad u_r = (ik_0/2)(\hat{X} - \tfrac{1}{4}\hat{X}^2)u, \tag{14a}$$

where the operator

$$\hat{X} = \frac{1}{k_0^2}\frac{\partial^2}{\partial z^2} + n^2(r,z) - 1 \tag{14b}$$

contains no θ dependence whatsoever.

Equations (12)–(14) represent a classification *mathematically* of propagation problems for the LSS equation into 3-D, $N\times$2-D, and 2-D cases. An important feature of the model is that all three cases are included within the mathematical formulation. We indicate below how all three cases are included implicitly within the numerical solution in FOR3D as well. We remark that the same classification could also be applied to more general propagation models. For instance, instead of referring to the LSS Eq. (4), here are the corresponding equations for the two-way equation (3):

$$\text{3-D:}\quad u_{rr} + 2ik_0u_r + u_{zz} + (1/r^2)u_{\theta\theta} + k_0^2[n^2(r,\theta,z) - 1]u = 0, \tag{15a}$$

$$N\times\text{2-D:}\quad u_{rr} + 2ik_0u_r + u_{zz} + k_0^2[n^2(r,\theta,z) - 1]u = 0, \tag{15b}$$

$$\text{2-D:}\quad u_{rr} + 2ik_0u_r + u_{zz} + k_0^2[n^2(r,z) - 1]u = 0. \tag{15c}$$

We now indicate a classification *computationally* for the 3-D, $N\times$2-D, and 2-D propagation problems within FOR3D. The three-point central differencing for the operator Y in Eq. (11) leads to a symmetric tridiagonal system matrix B, with diagonal elements $1 + 2s$ and upper and lower diagonal elements $-s$, where

$$s = \frac{i}{4}\frac{\Delta r}{k_0 r^2(\Delta\theta)^2}. \tag{16}$$

That is, each row of Bu^{j+1}, excluding those with boundary terms, has the form

$$(Bu^{j+1})_m = -su^{j+1}_{m,l+1} + (1+2s)u^{j+1}_{m,l} - su^{j+1}_{m,l-1}. \tag{17}$$

Note that in the 2-D case, where θ variation of u is negligible, we have $u^{j+1}_{m,l+1} = u^{j+1}_{m,l} = u^{j+1}_{m,l-1}$, so that the right side of Eq. (17) reduces to Iu^{j+1}_m, where I is the identity matrix. In the $N\times$2-D case when θ coupling is negligible, the near equalities of $u^{j+1}_{m,l+1}$, $u^{j+1}_{m,l}$, and $u^{j+1}_{m,l-1}$ will cause B to very closely approximate I. In both cases, Eq. (11) reduces to u^{j+1} and w^{j+1}, and only Eq. (10) needs to be solved [in the $N\times$2-D case, Eq. (11) is an uncoupled set of N tridiagonal subsystems]. We also note that for small s, Eq. (17) reduces approximately to Iu^{j+1}_m. Therefore, a choice of $\Delta\theta$ large, giving sufficiently small s, will approximate the solution of the $N\times$2-D case. Further, choosing $\Delta\theta$ small will produce θ coupling in the solution if that effect is, in fact, present in the propagation problem under consideration. On the other hand, if θ coupling is not present in the problem, then even choosing $\Delta\theta$ small will not produce a solution that differs significantly from the $N\times$2-D case. In such a situation, the finite-difference approximation for the operator Y will differ negligibly from zero, so that the matrix B will be effectively the identity.

In summary, the computational classification of problems begins with the 3-D case of Eq. (9), and the others are

$$N\times\text{2-D:}\quad \left[1 + \left(\frac{1}{4} - \frac{\delta}{4}\right)X\right]Iu^{j+1} = \left[1 + \left(\frac{1}{4} + \frac{\delta}{4}\right)X\right]Iu^j, \tag{18a}$$

$$\text{2-D:}\quad \left[1 + \left(\frac{1}{4} - \frac{\delta}{4}\right)\hat{X}\right]Iu^{j+1} = \left[1 + \left(\frac{1}{4} + \frac{\delta}{4}\right)\hat{X}\right]Iu^j, \tag{18b}$$

where the operator X depends on θ in Eq. (18a) but $\hat{X}$ does not in Eq. (18b). Flexibility in the choice of the parameter s allows θ-coupling to be examined, as indicated above.

Finally, we describe a classification *physically* for the 3-D, $N\times$2-D, and 2-D situations. In the 2-D case of Eq. (14), there is no variation with θ in the acoustic pressure. Along a mean wave front r = constant, there would be no variation in the acoustic field. This circumstance is one of no horizontal refraction. In the $N\times$2-D case, we consider Eq. (13), along with its complex conjugate, and form a so-called energy equation in the usual manner. If we then integrate the resulting equation over depth from the surface $z = 0$ to the base $z = z_A$ of the (artificial) bottom layer, and use boundary conditions $w = 0$ at both depths, the result is

$$N\times\text{2-D:}\quad \frac{\partial}{\partial r}\int_0^{z_A} |u|^2\,dz = 0, \tag{19a}$$

where vertical bars denote complex magnitude. Equation (19a) is known to be a statement of the conservation law for our parabolic approximation which corresponds to conservation of acoustic energy.[18,19] Since our Eq. (13) does not include density variations or attenuation processes explicitly, these mechanisms are absent in Eq. (19a) also, although extensions to include them are possible. Within the context of our parabolic approximation, Eq. (19a) is correctly interpreted as stating that the depth average of (the approximation for) acoustic energy in any vertical plane is constant in

range. It follows that energy in any vertical plane $\theta =$ constant is preserved as the acoustic wave propagates. Therefore, no net energy is exchanged between vertical planes in the absence of θ coupling, as noted previously for the narrow-angle version of Eq. (13).[2] From Eq. (19a), in the particular case when the source happens to be axisymmetric, i.e., omnidirectional for 360° field width, the depth-averaged acoustic energy is the same at *any* horizontal position (r,θ). We also remark that both amplitude and phase of the acoustic field can vary with θ, as a result of horizontal refraction of wavefronts due to $n^2(r,\theta,z)$. It is appropriate to interpret the case of no θ coupling as one with horizontal refraction but with no net energy exchange between vertical planes. Finally, in the 3-D case with θ coupling, the solution of Eq. (12) does not satisfy Eq. (19a), but can easily be shown instead to satisfy:

$$\text{3-D:}\quad \frac{\partial}{\partial r}\int_0^{2\pi}\int_0^{z_A}|u|^2\,dz\,d\theta = 0. \tag{19b}$$

This result corresponds to conservation of acoustic energy within the parabolic approximation generally and our restrictions (such as constant density) specifically. While depth-averaged energy need no longer be preserved within any given plane $\theta =$ constant, it must be preserved considering all azimuthal planes. Therefore, the case of θ coupling can be interpreted as admitting both horizontal refraction *and* net energy exchange between vertical planes.

III. COMPUTATIONAL EXAMPLES WITH ANALYTICAL SOLUTIONS

In this section and the next, we present computational results that demonstrate the accuracy and capabilities of the research code FOR3D. We focus in the section on tests with a family of analytical solutions to parabolic approximations that have been determined.[20] Members of the set can be constructed to satisfy the LSS Eq. (4) for particular indices of refraction and can be selected to satisfy convenient boundary conditions. Advantages of these solutions include the following: (1) They represent exact solutions to the parabolic approximations, and therefore can be useful in checking accuracy of computed solutions. (2) They model effects of horizontal refraction, using reasonable parameters and sound speed values. Thus, for example, they can be used to appraise model capability for treating θ-coupling. (3) They can be constructed with elementary functions that are convenient to evaluate and display. (4) They can be constructed so as to be simple approximate solutions for other propagation models, and thereby possibly be useful for model comparisons.

Details of derivations and descriptions of other results may be found in Ref. 20. We first consider an example designed to test accuracy and to illustrate effects of θ coupling. A second example is presented to illustrate the influence of conditions on the side boundaries of the computational domain.

A. Accuracy validation

The formula for a solution $u(r,\theta,z)$ of Eq. (4) with boundary conditions $u(r,\theta,0) = 0$ and $u_z(r,\theta,H) = 0$ is

$$u = \sin[(j+1/2)\pi z/H]\sin[\beta_0 k_0(\theta - \alpha_0 \log r)]$$
$$\times\exp\{ik_0 r[\alpha_0\theta - (j+1/2)^2(\pi k_0/H)^2/2]\}, \tag{20}$$

where j, H, α_0, β_0, and (as usual) $k_0 = 2\pi f/c_0$ are constants. Equation (20) holds for $0 < r_0 \leqslant r \leqslant r_{\max}$, $\theta_L \leqslant \theta \leqslant \theta_R$, and $0 \leqslant z \leqslant H$, provided $\theta_R - \theta_L < 2\pi$. For the narrow angle LSS equation, the corresponding index of refraction is

$$n^2(r,\theta) = 1 + \alpha_0^2 + 2\alpha_0\theta + \beta_0^2/r^2. \tag{21}$$

Note that as r increases, the last term in Eq. (21) becomes small. Consequently, n^2 tends to a linear function of θ, so the medium possesses a mechanism for horizontal refraction and possibly for θ coupling. Isospeed contours for Eq. (21) tend to spiral as r decreases.

We performed computations with FOR3D using Eq. (21) and compared the results numerically with both field values and decibel propagation losses from Eq. (20). Subsidiary conditions at $r = r_0$, $\theta = \theta_L - \Delta\theta$, and $\theta = \theta_R + \Delta\theta$ were taken as exact values from Eq. (20). Acoustical and computational parameter values for one of our calculations are given in Table I. Most of the symbol meanings are self-evident; all are defined in Refs. 7 and 21. Note that as with our parameter choices, the sound-speed variation with θ in the wedge-shaped domain is larger than typical cross-range gradients in ocean fronts and eddies. For example, at a radius of 3 km, $r^{-1}\,\partial c/\partial\theta$ is about 2.5 m/s per km. We performed other computations with both smaller, more typical gradients and larger ones. We present this particular case to illustrate how FOR3D handles a relatively challenging example.

The results for one range and azimuth location and for seven receiver depths are shown in Table II. The first line at each depth shows computations from FOR3D with angular increment 30°, i.e., with five sectors from θ_L to θ_R. These results are identical to those from $N\times$2-D calculations, i.e., with step 2 of Eq. (11) suppressed. This illustrates agreement between calculations ($B = I$), as discussed in Sec. II. In addition, results not shown here from the 2-D model IFD[21] are nearly identical to the $N\times$2-D calculations. This is to be expected, although differences are conceivable because IFD does not solve Eq. (14a).

The second line at each depth shows results from FOR3D with angular increment 1 deg, i.e., with 120 sectors from θ_L to θ_R. Note first the differences from the $N\times$2-D results. This demonstrates that θ coupling is in fact occurring in this example. Its clear presence here is a result of the large cross-range sound-speed gradient mentioned earlier. Next, note the very close agreement, nearly always to three

TABLE I. Parameter values for numerical computations with analytical solution.

$\alpha_0 = 0.005$	$c_0 = 1500$ m/s	$\theta_L = 30$ deg
$\beta_0 = 100$ m	$f = 50$ Hz	$\theta_R = 150$ deg
$j = 0$	$H = 40$ m	$r_0 = 500$ m
$\Delta z = 1$ m	$z_s = 20$ m	$r_{\max} = 5000$ m
$\Delta r = 20$ m		

TABLE II. Comparison of FOR3D computations and exact solutions: $r = 3000$ m, $\theta = 90$ deg.

Receiver depth (m)	Solution u Real part	Imag. part		Propagation loss (dB)
5	−0.17380	−0.04514	$\Delta\theta = 30$ deg	49.69
	−0.13503	0.00726	$\Delta\theta = 1$ deg	52.15
	−0.13488	0.00663	Exact	52.16
10	−0.34142	−0.07978	$\Delta\theta = 30$ deg	43.88
	−0.26477	0.01418	$\Delta\theta = 1$ deg	46.30
	−0.26458	0.01300	Exact	46.31
15	−0.48832	−0.10418	$\Delta\theta = 30$ deg	40.80
	−0.38433	0.02048	$\Delta\theta = 1$ deg	43.07
	−0.38411	0.01887	Exact	43.07
20	−0.60757	−0.11816	$\Delta\theta = 30$ deg	38.94
	−0.48913	0.02591	$\Delta\theta = 1$ deg	40.97
	−0.48888	0.02402	Exact	40.98
25	−0.68989	−0.11477	$\Delta\theta = 30$ deg	37.88
	−0.57513	0.03017	$\Delta\theta = 1$ deg	39.56
	−0.57486	0.02824	Exact	39.57
30	−0.72780	−0.08489	$\Delta\theta = 30$ deg	37.47
	−0.63900	0.03293	$\Delta\theta = 1$ deg	38.65
	−0.63875	0.03138	Exact	38.65
35	−0.72587	−0.03334	$\Delta\theta = 30$ deg	37.55
	−0.67826	0.03418	$\Delta\theta = 1$ deg	38.13
	−0.67809	0.03331	Exact	38.13

digits, between the second and third lines of results. The latter are evaluations of the exact solution Eq. (20). These demonstrate (a) the high accuracy that can be obtained with FOR3D, and (b) the capability of FOR3D in treating θ coupling when it exists. We have performed many such tests, a few others of which appear in Ref. 20. They confirm the accuracy of FOR3D.

B. Side boundary condition influences

In applications of FOR3D, an issue is what conditions to impose on side boundaries of the computational domain. For example, in Sec. III A the exact solution values were imposed at one computational step $\Delta\theta$ outside the side boundaries at $\theta = \theta_L$ and $\theta = \theta_R$. Normally, the exact fields would not be available for use as boundary conditions. Another possibility is to enlarge the domain into a full 360 deg about the source. This may require determining many more field values than are desired, and in any case is computationally prohibitive now for ranges of interest. An additional method would be to construct artificial absorbing boundaries at the domain sides, analogous to those used at the base of sediment layers in all parabolic approximation algorithms. This capability is available for user input to FOR3D.

In practice, we have adopted another procedure for selection of side boundary conditions, based upon the following idea. Suppose that a sequence of boundary conditions is constructed for a well-posed initial-boundary value problem for a partial differential equation such as LSS, and that a sequence of solutions are obtained corresponding to each of the boundary conditions. Suppose further that the former sequence converges, in some appropriate sense, to a desired exact boundary condition. Then we would expect that the sequence of solutions converges in an appropriate sense to the solution of the problem with the limiting boundary condition. The mathematical justification of this procedure for the LSS equation will be presented elsewhere. We apply the idea by constructing just the first boundary conditions of a sequence, specifically by computing $N \times 2$-D solutions at one computational step beyond the vertical side boundaries. In so doing, if θ coupling is present at the boundary, the solution obtained cannot be correct in the entire computational domain. (If no θ coupling is present at the boundary, the solution could be determined correctly in the entire domain.) Previous computations, as for example in Ref. 8, have illustrated how effects of improper side boundary conditions can partially corrupt the correct solution away from the boundaries. The question is whether this procedure provides the correct 3-D solution in some (or any) azimuthally restricted subdomain that is sufficiently wide to be worthwhile. If so, the situation is analogous to the case of requiring extra computation in an enlarged domain using artificial side absorbing boundaries, inside which the solution is incorrect. Observations of computations using FOR3D have been that the answer is yes, and quantitative analysis will be given elsewhere.

To validate the procedure, we employ the analytical solution as a benchmark. We describe one set of computations which use the same parameters as in Table I, except $\theta_L = -60$ deg, $\theta_R = 60$ deg, $\Delta\theta = 1$ deg (and smaller for verification), initial range 1 km, and maximum range extended to 30 km. One calculation was made with the exact solution values at $\theta = \theta_L - \Delta\theta$ and $\theta = \theta_R + \Delta\theta$. Another was made with $N \times 2$-D solution values at the side locations. Since Sec. III A shows that strong θ coupling occurs in this example, the 2-D boundary conditions are only approximations to the correct ones. Figure 1 shows solutions at three vertical sections of the 120-deg wedge domain. Solutions at each of the azimuths 36 and 39 deg are identical for the two boundary conditions. Note the deep fade in the 36-deg solution, which is an example of a pattern that requires an accurate 3-D computation to resolve.[20] There is a barely discernible difference between solutions from the two calculations in the plane $\theta = 42$ deg. Vertical sections closer to the boundary at 60 deg are shown in Fig. 2. Differences are pronounced beyond about 3 km in the lower pair of curves, for 45 deg. The spurious oscillations indicate that influences of the 2-D boundary conditions have penetrated to the domain interior. Note that the deep fade before 2 km is resolved correctly, even with 2-D boundary conditions. In the upper pair of curves, for 48 deg, differences between calculations for the two cases appear to arise earlier in range than for the 45-deg case. This trend is confirmed in Fig. 3, in which solu-

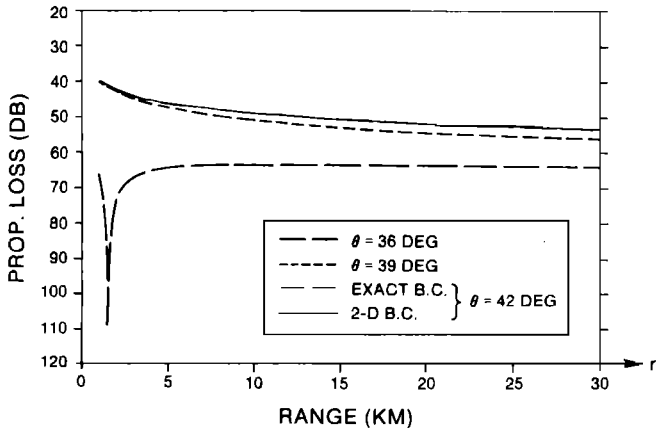

FIG. 1. Propagation loss versus range; sound speed from Eq. (21) and parameters from Table I. Curves show little or no effect of side boundary conditions.

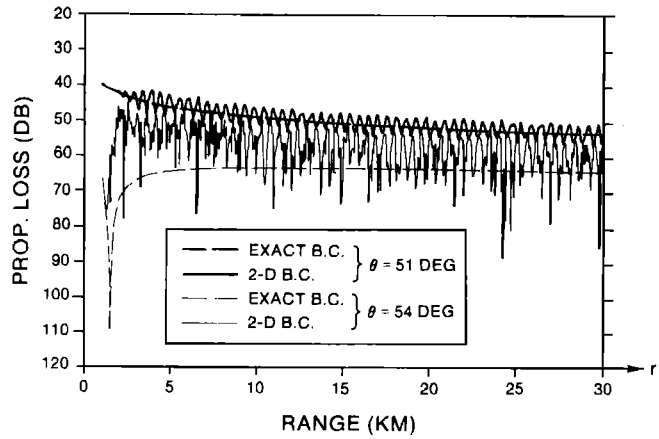

FIG. 3. Propagation loss versus range; same as Fig. 2 but closer to side boundary.

tions shortly beyond 1 km are fatally compromised by incorrect 2-D side conditions. Note that the early deep fade for $\theta = 54$ deg is not computed correctly with 2-D boundary conditions.

Results of these calculations are summarized in the plan view of the domain shown in Fig. 4. Agreement between the solutions computed with exact 3-D or approximate 2-D boundary conditions is indicated in a subdomain extending over 80 deg in azimuthal width. Solution "match" was taken as agreement in the complex fields of at least two significant digits. The shaded subdomain indicates where this criterion was not satisfied. The borders between the two subdomains is neither a single radial line from the origin nor exactly symmetric with respect to the origin. The key point is that the correct 3-D solution is obtained in a substantial subdomain, even though approximate conditions are used at side boundaries. In other words, the approximate boundary conditions do not penetrate too deeply into the domain, even in this example where strong θ coupling is known to occur at the boundaries. The essential reason for success of the procedure is that θ coupling effects characteristic of the real ocean

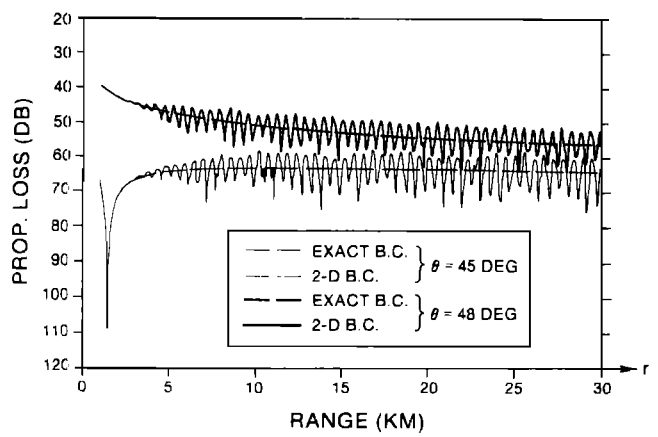

FIG. 2. Propagation loss versus range; same model as Fig. 1. Curves show strong dependence on side boundary conditions.

can be non-negligible but are not substantial. That is, artificial examples with very strong θ coupling can be constructed to corrupt even the solution at $\theta = 0$. Also, recall that the cross-range sound-speed gradient for Fig. 4 computations is large for small range and has decreased to about 1 m/s per km near 10-km range. Hence, the extent of penetration here may be larger than might be anticipated from actual ocean conditions.

IV. COMPUTATIONAL EXAMPLES WITH A MODEL OCEAN ENVIRONMENT

We next describe computations with FOR3D that employ a representation of the three-dimensional ocean sound-speed field and bottom topography. In order to illustrate a situation with θ coupling present, a location was selected where variations in ocean bottom topography occur. The initial version of FOR3D, as documented in Ref. 7, did not have the capability to treat bottom variations. This capability has now been incorporated, and initial accuracy tests have been performed.[9] The details of the implementation will be reported elsewhere, along with other enhancements. A representation of bottom topography, showing constant-depth contours, in a region of the Atlantic is shown in Fig. 5. This was obtained from Harvard University oceanographers, who employ these and other bottom data with forecasts in a 900×1950-km ocean domain from an enhanced version of the Harvard open ocean model (HOOM).[22,23] Also shown is the source location and the wedge-shaped domain of acoustic propagation. Note that the domain straddles a region of significant topographical variation, from continental slope on the left boundary (view from the source in the propagation direction), $\theta = \theta_L = 140$ deg, to continental shelf on the right boundary, $\theta = \theta_R = 220$ deg.

Sound-speed values were provided by a forecast of 3 October 1988 from the HOOM. This particular case consists of data at six levels in the vertical (100, 300, 700, 1100, 2200, and 3900 m) on a square grid with size 15 km. Sound-speed information is processed for use in FOR3D in the same manner as in the use of the IFD model.[24] Other propagation

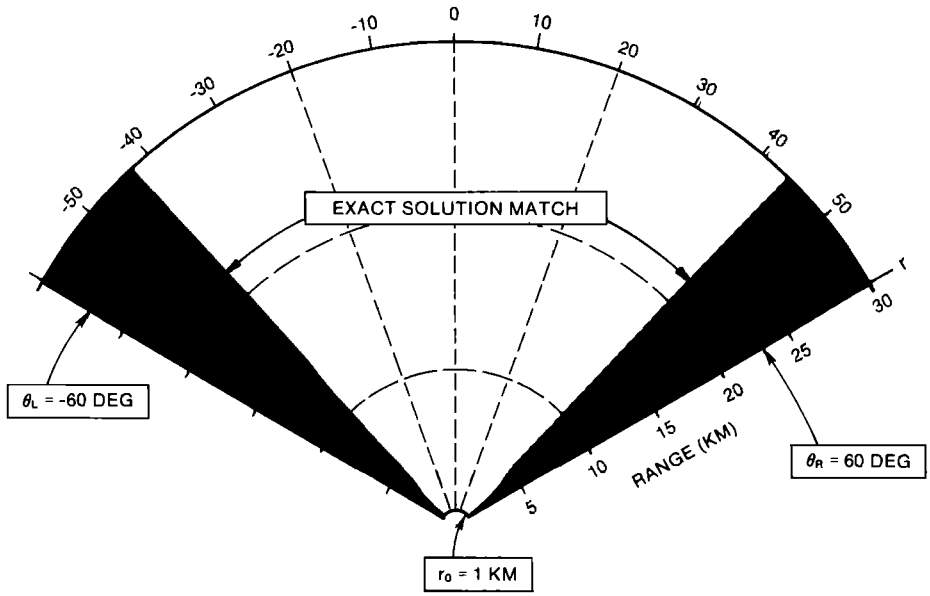

FIG. 4. Horizontal domain for analytical solution calculations, indicating where solutions are independent of (unshaded) and dependent upon (shaded) side boundary conditions.

studies[25–27] have exploited HOOM sound-speed forecasts based on six vertical levels. Other investigations, such as Ref. 28, have indicated the importance for low-frequency acoustic propagation results of increasing the number of vertical levels. Consequently, we emphasize that the sound-speed values are not to be regarded as accurate forecasts in this region of the model domain. Rather, the profiles can be considered as typical of the mean sound speed which might be expected in the propagation region. Figure 6 shows sections through the center [Fig. 6(b)] and both boundaries of the wedge. The sketches include both sound-speed and bottom topography. We note that among previous investigations of interfacing between HOOM output and parabolic approximation models to date, only Ref. 26 has demonstrated and discussed the importance of including topography in both ocean and acoustic models. The ocean channel is modeled

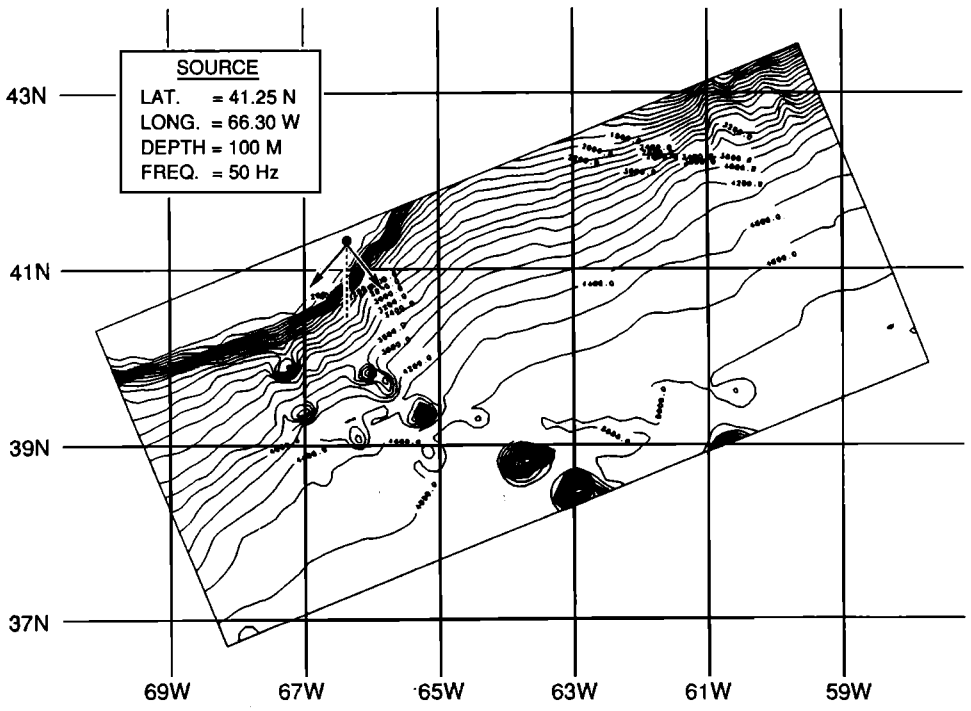

FIG. 5. Source location, propagation domain, and level curves of bottom topography; contour interval 200 m.

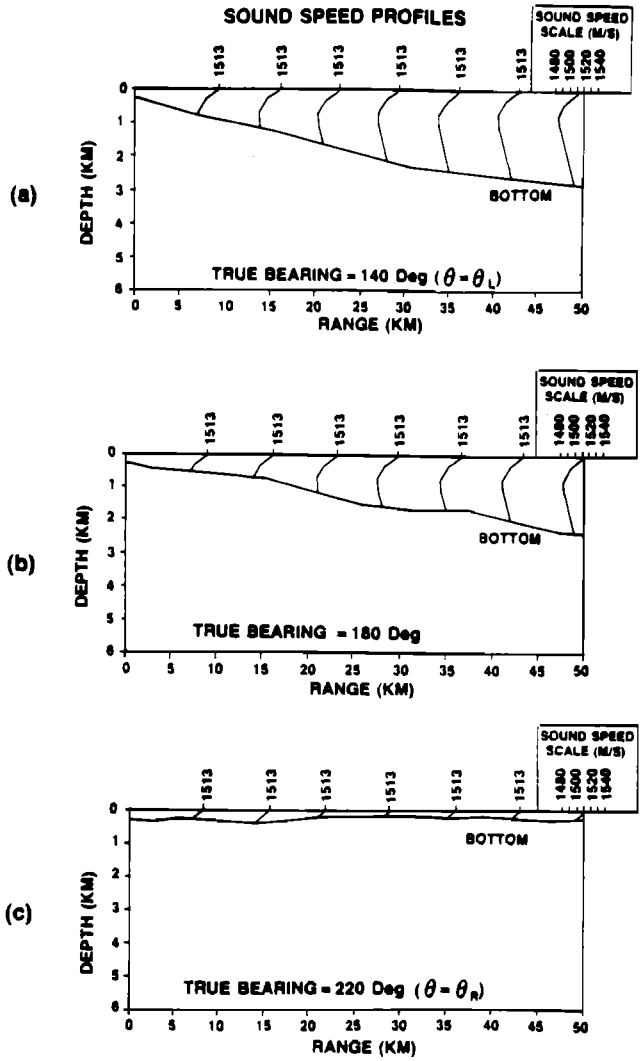

FIG. 6. Bottom topography and representative sound speed profiles along vertical sections: (a) east boundary, (b) center line, (c) west boundary.

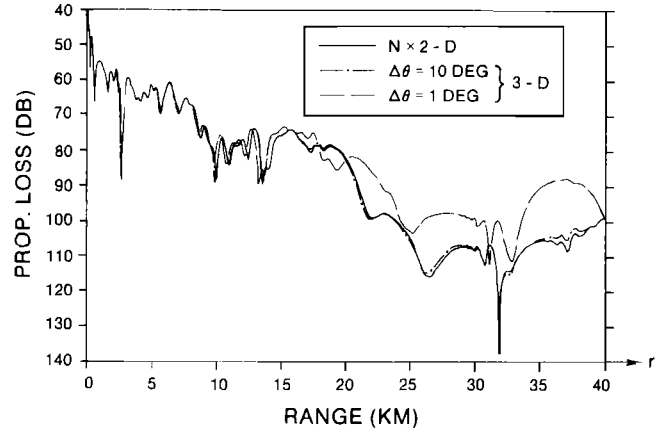

FIG. 7. Propagation loss versus range from FOR3D for Figs. 5 and 6 example: $N \times 2$-D and nonconvergent 3-D solutions; $z_s = 100$ m, $\theta = 180$ deg.

for the acoustic computations by including the given sound-speed profiles and bottom topography as suggested by Fig. 6. A sediment layer of thickness 100 m is added below the bottom interface. The sediment sound speed is 1.005 times the value of water sound speed at the interface, a sound-speed gradient of 1.9/s is maintained in the layer, and sediment attenuation is 0.1 dB per wavelength. In these initial computations sediment density ρ_B is kept at 1 g/cm^3. The depth interval below the sediment layer is filled with an artificial absorbing layer with the same value of sound speed as at the base of the sediment layer. The ocean surface is taken as pressure release. The solutions at the side boundaries are computed from the 2-D side boundary option of FOR3D, i.e., using Eq. (19a), in the procedure described in Sec. III B. The initial condition is an azimuthally symmetric Gaussian starting field. Computational values $\Delta r = 2$ m, $\Delta z = 2$ m, and $c_0 = 1500$ m/s were used; tests were performed to be certain that range and depth increments were small enough to assure convergence.

In Fig. 7 results from three FOR3D calculations of propagation loss are presented for ranges out to 40 km. We note that results for longer ranges show the same general characteristics (computations beyond 200 km have not been performed). In this and subsequent figures, the receiver depth is 100 m, and the plane of propagation corresponds to the center line of the wedge domain, $\theta = 180$ deg. The dashed curve is the $N \times 2$-D calculation with Eq. (11) suppressed, and $N = 9$ in this case. The general shape is not unexpected for downslope propagation, although the intensity level appears to drop quite quickly as range increases past 20 km, with an upward trend after 35 km. The dashed–dot curve is a 3-D calculation with $\Delta\theta = 10$ deg, i.e., with the same number of sectors as the solid curve. The two curves coincide out to 20 km, and differ only slightly beyond 20 km. The agreement illustrates the important correspondence between an $N \times 2$-D calculation and one with FOR3D with large angular increment. That is, performing the 3-D calculation with azimuthal increments large enough to suppress θ coupling produces nearly identical results as the $N \times 2$-D procedure. The (light) long-dashed curve is the FOR3D calculation with azimuthal increment $\Delta\theta = 1$ deg. This curve nearly coincides with the other two out to 10 km. Beyond that range a small phase shift appears, and by 20 km, patterns of the two 3-D calculations differ markedly. The comparison confirms the existence of substantial θ coupling in this domain with bottom topographical variations. Implicit in the conclusion is that the approximate ($N \times 2$-D) side boundary conditions do not corrupt the solution at the center of the domain. In view of Sec. III B, we have confidence that this assumption is correct; it can be verified by perturbing the side boundary conditions, in amounts consistent with field differences in the two FOR3D cases, for the $\Delta\theta = 1$-deg case and checking that solutions at the center of the wedge are unchanged.

Although azimuthal coupling has been demonstrated to occur, can we be certain that the long-dashed curve in Fig. 7 gives an accurate solution? That is, has the FOR3D solution for $\Delta\theta = 1$ deg effectively converged? A straightforward procedure for numerical demonstration of convergence is to continually refine the azimuthal increment until field solutions do not change. A calculation for $\Delta\theta = 1/2$ deg was

performed and showed observable differences beyond 20 km, verifying that convergence has not been reached. Continued halving of the azimuthal increment is expensive in computational time and memory. Consequently, an alternative method was used. This method is motivated by the robustness of solutions at the domain center to conditions imposed at the side boundaries, as discussed earlier, and by the apparently limited azimuthal spread of influence of θ-coupling effects in typical ocean situations. We consider a wedge domain of smaller extent, specifically with $\theta_L = 175$ deg and $\theta_R = 185$ deg. Computations were performed with FOR3D in this restricted domain with $\Delta\theta = 1$ deg and 1/2 deg. The resulting solutions are the same (to at least three significant figures) as those in the larger domain of width 80 deg. The light long-dashed and short-dashed curves in Fig. 8 show these solutions, with the former being the same curve as in Fig. 7. The agreement between solutions in the larger and smaller domains demonstrates that the center solution has not been contaminated by the side conditions, even in the narrow domain. (However, use of a very narrow domain of width 1 deg did show contamination of the center solution for small $\Delta\theta$ values.) Consequently, the method is to refine the azimuthal increment in the smaller domain until convergence is reached. The heavy curves in Fig. 8 show the next refinements for $\Delta\theta = 1/4$ deg and 1/8 deg. The heavy solid curve overlays the curve (not shown) for $\Delta\theta = 1/16$ deg, which indicates that convergence has occurred for the 1/8 deg calculation.

The main results for the computation are summarized in Fig. 9. The light curve is the same 2-D solution as in Fig. 7, and the heavy curve is the same convergent 3-D solution as in Fig. 8. Beyond 20-km intensity differences are large, up to 15 dB, apart from even larger differences associated with the deep fade near 32 km. Generally the 3-D calculation has significantly higher intensity in this example. These results not only confirm the occurrence of azimuthal coupling but also present its quantitative influence, within the assumptions of the propagation model and its implementation.

An additional example is displayed in Fig. 10. For this

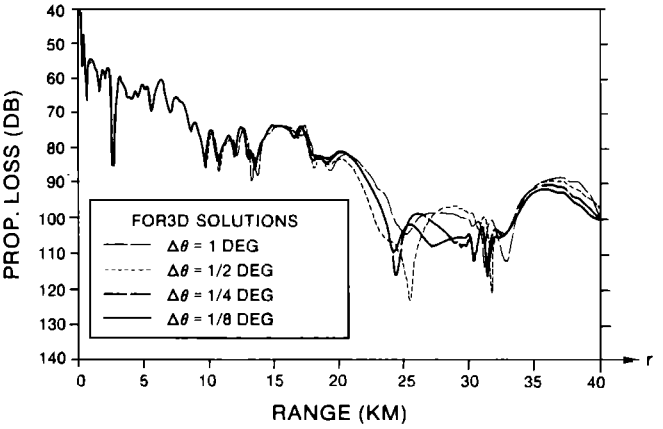

FIG. 9. Propagation loss versus range from FOR3D; same as Fig. 7 but comparing $N \times 2$-D and convergent 3-D solutions.

case, the density in the sediment layer is taken as 1.7 g/cm^3. The modifications to the FOR3D implementation in order to incorporate this physical effect are discussed in Ref. 9. The curves in Fig. 10 indicate the changes in the FOR3D solution as θ is refined in the smaller wedge domain. As before, the solutions for $\Delta\theta = 1$ deg and 1/2 deg agree with those in the original larger domain, and also the solutions in the smaller domain for $\Delta\theta = 1/8$ deg and 1/16 deg overlay. The comparison between the convergent 3-D solution (heavy curve) and the $N \times 2$-D solution (light curve) is shown in Fig. 11. There are significant intensity differences between the two curves, verifying that θ coupling does occur in this example. The 3-D intensity is well above the 2-D intensity near 20 km, but the situation is reversed near 35 km. A primary conclusion is that in comparing Figs. 9 and 11, we see comparable intensity differences between the 2-D and 3-D solutions in both cases. Thus, the inclusion of sediment density appears to change details of the θ-coupling effect but not its overall order of magnitude. Results for other receiver and source locations support this conclusion.

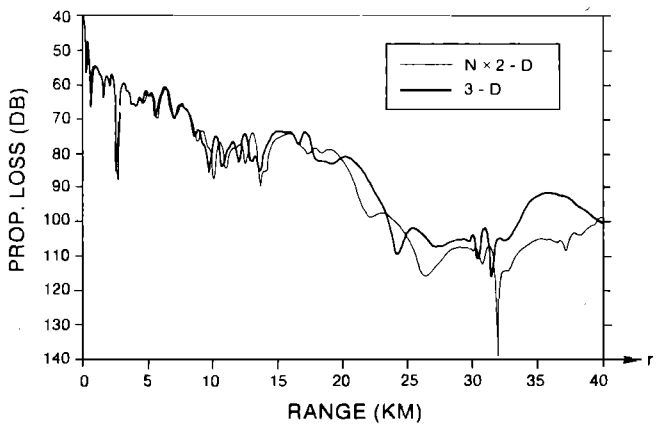

FIG. 8. Propagation loss versus range from FOR3D; same as Fig. 7 but showing convergence of 3-D solutions.

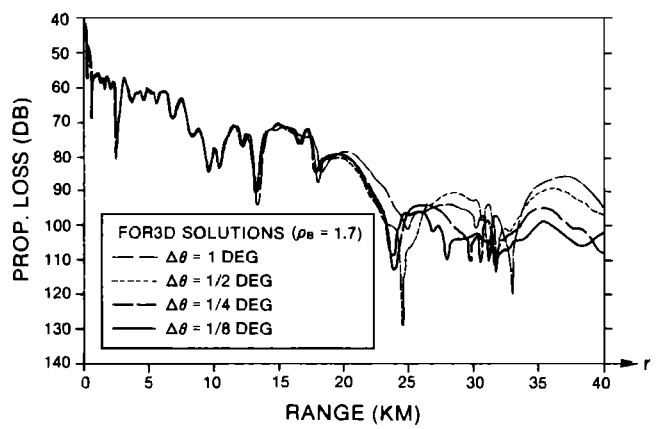

FIG. 10. Propagation loss versus range from FOR3D; same as Fig. 8 but with sediment density difference included.

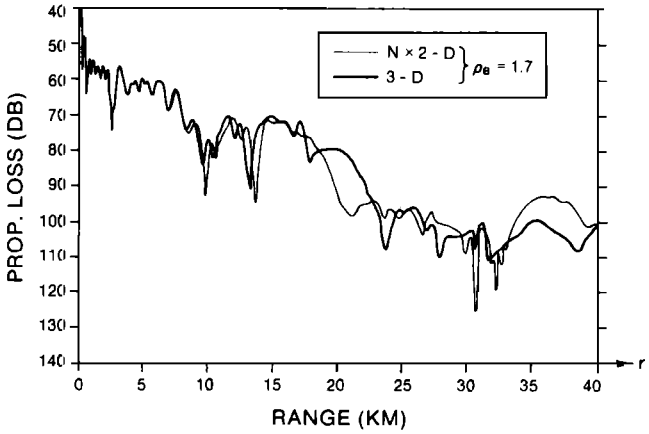

FIG. 11. Propagation loss versus range from FOR3D; same as Fig. 9 but with sediment density difference included.

V. CONCLUSIONS

In treating the prediction of 3-D ocean acoustic propagation, the mechanism of θ coupling is important in some situations. If θ coupling is present, its treatment would call for the use of a fully 3-D model. If θ coupling is weak or absent, accurate 2-D models may be applied to process the prediction in N different sectors, for which case the terminology $N \times$2-D has been used. In this paper, we first reviewed the background and features of the FOR3D model. Then, 3-D, $N \times$2-D, and 2-D propagation cases were discussed mathematically, computationally, and physically using the model. In order to establish its accuracy and to demonstrate its capability for handling θ coupling, we performed an analytic solution test. An exact solution of the propagation equation which is the basis of FOR3D was used. Both high accuracy and full θ coupling occur for computations with sufficient azimuthal resolution. The exact solution was used to validate a procedure for using approximate ($N \times$2-D) conditions at the vertical side boundaries in a 3-D calculation. The correct 3-D solution is determined in a subdomain of the original domain. Then, an application of FOR3D was made to an ocean environment with realistic bottom topography and sound-speed profiles, obtained from the Harvard University oceanography group. A propagation region on the Atlantic shelf-slope region was examined. A methodology for assuring numerical convergence of 3-D propagation solutions was discussed. The occurrence of substantial θ coupling was demonstrated in the domain with significant bottom variations. In a situation such as this, only accurate 3-D propagation models should be used, rather that $N \times$2-D models. It is apparent that not every 3-D ocean acoustics problem can be adequately solved by 2-D propagation models.

ACKNOWLEDGMENTS

Model ocean data from Harvard Gulfcasts were generously provided by Professor Allan Robinson and Dr. Scott Glenn. The authors appreciate conversations with Dr. Paul Scully-Power during the course of this work, as well as comments from Dr. Michael D. Collins. Initial phases of this research were performed under the sponsorship of the Naval Underwater Systems Center (Independent Research Project A65020), Office of Naval Research (Contract No. N00014-88-WX-24160), and Institute for Naval Oceanography (Subcontract No. S8756). Later work was completed under the sponsorship of the Office of Naval Research (Contracts No. N00014-86-K-0129, N00014-88-WX-24160, and N00014-91-J-1033).

[1] R. N. Baer, "Propagation through a three-dimensional eddy including effects on an array," J. Acoust. Soc. Am. **69**, 70–75 (1981).
[2] J. S. Perkins and R. N. Baer, "An approximation to the three-dimensional parabolic-equation method for acoustic propagation," J. Acoust. Soc. Am. **72**, 515–522 (1982).
[3] M. J. Buckingham, "Theory of three-dimensional acoustic propagation in a wedgelike ocean with a penetrable bottom," J. Acoust. Soc. Am. **82**, 198–210 (1987).
[4] M. D. Collins and S. A. Chin-Bing, "Three-dimensional sound propagation in shallow water including the effects of rough surfaces," in *Computational Acoustics: Seismo-Ocean Acoustics and Modeling*, edited by D. Lee, A. Cakmak, and R. Vichnevetsky (North-Holland, Amsterdam, 1990), pp. 247–259.
[5] M. D. Collins and S. A. Chin-Bing, "A three-dimensional parabolic equation model that includes the effects of rough boundaries," J. Acoust. Soc. Am. **87**, 1104–1109 (1990).
[6] D. Lee, Y. Saad, and M. H. Schultz, "An efficient method for solving the three-dimensional wide angle wave equation," in *Computational Acoustics: Wave Propagation*, edited by D. Lee, R. L. Sternberg, and M. H. Schultz (North-Holland, Amsterdam, 1988), pp. 75–90.
[7] G. Botseas, D. Lee, and D. King, "FOR3D: A computer model for solving the LSS three-dimensional wide angle wave equation," Naval Underwater Systems Center, New London, CT, Tech. Rep. 7934 (1987).
[8] W. L. Siegmann, D. Lee, and G. Botseas, "Finite difference computations of three-dimensional sound propagation," in *Computational Acoustics: Wave Propagation*, edited by D. Lee, R. L. Sternberg, and M. H. Schultz (North-Holland, Amsterdam, 1988), pp. 91–109.
[9] D. Lee, M. H. Schultz, and Y. Saad, "A three-dimensional wide angle wave equation with vertical density variations," in *Computational Acoustics: Ocean-Acoustic Models and Supercomputing*, edited by D. Lee, A. Cakmak, and R. Vichnevetsky (North-Holland, Amsterdam, 1990), pp. 143–154.
[10] A. E. Newhall, J. F. Lynch, C. S. Chiu, and J. R. Daugherty, "Improvements in three-dimensional raytracing codes for underwater acoustics," in *Computational Acoustics: Ocean-Acoustic Models and Supercomputing*, edited by D. Lee, A. Cakmak, and R. Vichnevetsky (North-Holland, Amsterdam, 1990), pp. 169–185.
[11] J. S. Perkins, M. Williamson, W. A. Kuperman, and R. B. Evans, "Sound propagation through the Gulf Stream: Current status of two three-dimensional models," in *Computational Acoustics: Ocean-Acoustic Models and Supercomputing*, edited by D. Lee, A. Cakmak, and R. Vichnevetsky (North-Holland, Amsterdam, 1990), pp. 203–215.
[12] C. S. Chiu and L. L. Ehret, "Computation of sound propagation in a three-dimensionally varying ocean: A coupled normal mode approach," in *Computational Acoustics: Ocean-Acoustic Models and Supercomputing*, edited by D. Lee, A. Cakmak, and R. Vichnevetsky (North-Holland, Amsterdam, 1990), pp. 187–202.
[13] R. B. Evans, "Three dimensional acoustic scattering from a cylindrical inclusion in a waveguide," in *Computational Acoustics: Scattering, Gaussian Beams, and Aeroacoustics*, edited by D. Lee, A. Cakmak, and R. Vichnevetsky (North-Holland, Amsterdam, 1990), pp. 123–132.
[14] S. A. Chin-Bing, "Acoustic wavefield distortion by seamounts: A finite element analysis," in *Computational Acoustics: Ocean-Acoustic Models and Supercomputing*, edited by D. Lee, A. Cakmak, and R. Vichnevetsky (North-Holland, Amsterdam, 1990), pp. 37–52.
[15] J. A. Fawcett and T. W. Dawson, "Fourier synthesis of three-dimensional scattering in an oceanic waveguide using two-dimensional boundary integral methods," J. Acoust. Soc. Am. **88**, 1913–1920 (1990).
[16] W. L. Siegmann, G. A. Kriegsmann, and D. Lee, "A wide-angle three-dimensional wave equation," J. Acoust. Soc. Am. **78**, 659–664 (1985).

[17] L. E. Estes and G. Fain, "Numerical techniques for computing the wide-angle acoustic field in an ocean with range-dependent velocity profiles," J. Acoust. Soc. Am. **62**, 38–43 (1977).
[18] A. D. Pierce, "The natural reference wavenumber for parabolic approximations in ocean acoustics," Comp. Math. Appl. **11**, 831–841 (1985).
[19] M. B. Porter, F. B. Jensen, and C. M. Ferla, "The problem of energy-conservation in one-way models," J. Acoust. Soc. Am. **89**, 1058–1067 (1991).
[20] W. L. Siegmann, D. Lee, and G. Botseas, "Analytical solutions for testing accuracy and azimuthal coupling in three-dimensional propagation models," in *Computational Acoustics: Ocean-Acoustics Models and Supercomputing*, edited by D. Lee, A. Cakmak, and R. Vichnevetsky (North-Holland, Amsterdam, 1990), pp. 129–142.
[21] D. Lee and S. T. McDaniel, *Ocean Acoustic Propagation by Finite Difference Methods* (Pergamon, Oxford, 1988).
[22] A. R. Robinson and L. J. Walstad, "The Harvard Open Ocean Model: calibration and application to dynamical process, forecasting, and data assimilation studies," J. Appl. Numer. Math. **3**, 89–132 (1987).
[23] A. R. Robinson, S. M. Glenn, M. A. Spall, L. J. Walstad, G. M. Gardner, and W. G. Leslie, "Forecasting Gulf Stream meanders and rings," EOS: Oceanogr. Rep. **70**, 1464–1473 (1989).
[24] G. Botseas, D. Lee, and W. L. Siegmann, "IFD: Interfaced with Harvard Open Ocean Model forecasts," Naval Underwater Systems Center, New London, CT, Tech. Rep. 8367 (1989).
[25] A. R. Robinson, "Dynamical forecasting of mesoscale fronts and eddies for acoustical applications," J. Acoust. Soc. Am. Suppl. 1 **82**, S43 (1987).
[26] W. L. Siegmann, M. J. Jacobson, D. Lee, G. Botseas, A. R. Robinson, and S. M. Glenn, "Interfacing mesoscale ocean prediction and parabolic acoustic propagation models including bottom topography," in *Computational Acoustics: Ocean-Acoustic Models and Supercomputing*, edited by D. Lee, A. Cakmak, and R. Vichnevetsky (North-Holland, Amsterdam, 1990), pp. 155–168.
[27] L. E. Mellberg, A. R. Robinson, and G. Botseas, "Azimuthal variation of low-frequency acoustic propagation through asymmetric Gulf Stream eddies," J. Acoust. Soc. Am. **89**, 2157–2167 (1991).
[28] A. R. Robinson, S. M. Glenn, W. L. Siegmann, D. Lee, and G. Botseas, "Environmental sensitivity studies with an interfaced ocean-acoustics system," in *Ocean Variability and Acoustic Propagation*, edited by J. Potter and A. Warn-Varnas (Kluwer, Dordrecht, 1991), pp. 545–559.